Experimental Determination of Some Nonlinear Elements of Third Sound Dynamics

Ralph Baierlein, F. M. Ellis, and Hai Luo*

Department of Physics, Wesleyan University, Middletown, Connecticut 06459-0155, USA

The frequency shifts of third sound resonances during free decay are observed to have a quadratic dependence on the amplitude of the wave motion. An unambiguous measurement of amplitude allows for quantitative comparisons to predictions for the frequency shifts based on a variety of nonlinear influences acting within the superfluid ^4He film and resonator. Dispersive terms play a minor role in this analysis. We conclude that nonlinear terms dictated by a straight forward application of classical hydrodynamics are applicable to superfluid helium films.

INTRODUCTION

One of the remarkable features of superfluid helium films is the ease with which classical fluid mechanics can be adapted to the description of the dynamics. Within the two fluid model, the normal component is relatively inactive in a film, and the thermo-mechanical effects become negligible at low temperatures. The primary dynamical feature is third sound, the wave motion in films associated with longwave oscillatory displacements of the superfluid.[1] Third sound is consequently sensitive to the van der Waals attraction to the substrate, which acts as the restoring force, and to the superfluid density and film thickness, which dictate the inertial characteristics of the film's motion. Because of the microscopic thickness of the film, third sound is also easily within the longwave regime of the film dynamics—wavelengths are typically a million times greater than the film thickness.

This last point—the longwave regime—has been a source of inconsistency when the nonlinear aspects of the dynamics are considered. It is

---

*Present address: Medical Physics Program, East Carolina University, Greenville, North Carolina 27834, USA.

precisely the longwave regime that was expected to result in a nearly non-dispersive wave, enhancing the effects of the non-linear components in the mechanics. Soliton modes of propagation in superfluid ^{4}He films have been predicted, [2-4] based on the accepted hydrodynamic description of the films, but so far have not been clearly identified experimentally[5-8] in spite of this extreme longwave, low dispersion limit. All of the related experimental work in superfluids so far has been in the context of pulse propagation. It is the purpose of this paper to address some of the non-linear aspects of the dynamics with an experimental approach that is less ambiguous.

The source of the apparent inconsistency between the superfluid experiments and theory are two-fold. First are uncertainties in the appropriate dispersive influences acting in the longwave film. These have been discussed previously.[9] Several possible dispersive sources were proposed and estimated to be many orders of magnitude more influential than the traditional sources of surface tension and corrections to the longwave approximation (the force dispersion and intrinsic dispersion of Ref. 4). Among the most likely candidates are geometrical imperfections due to surface defects, unintentional deviations from rectangular wave geometry, or wavelength-dependent thermo-mechanical coupling.

The second contribution is experimental. Experiments searching for soliton-type behavior have involved third sound pulses which are interpreted in terms of many solitons as part of a train. A single soliton mode has never been clearly identified, as is easily done in shallow water. Based on traditional dispersions, the wave-length scale for solitons with amplitudes detectable by present techniques is quite small, typically sub-micron. It should be noted that there is an extensive body of literature related to nonlinear wave propagation in water and plasmas that suggest better techniques[10] for the interpretation of pulse-type third sound experiments.

We have taken a different approach by looking for non-linear influences in the more controlled environment of standing wave modes in a resonator. Our analysis is adopted from the water wave literature pertinent to resonant basins.[11] For the same reasons that solutions to the nonlinear equations of motion result in an amplitude-dependent wave speed, the experimental third sound resonances display an amplitude-dependent frequency. In a resonator, the wavelengths and frequencies form a discrete set, and therefore they are inherently well-defined and simpler to detect and to distinguish from the noise. In addition, because of the fairly high quality factors (Q's) at low amplitudes, extremely precise frequency measurements of these shifts are possible.

In these experiments, the relation between the frequency shift and the resonance amplitude can be followed over a wide range of amplitudes, from highly nonlinear to well into what is usually considered the linear regime.

Comparisons to the equations of motion can then be made in a limit where the approximations (small amplitude) are verifiably valid. We first consider the experimental aspects. These will indicate the level to which we need to carry the theory.

EXPERIMENTAL

The critical features of this experiment are the ability first, to accurately determine the amplitude and frequency of the third sound resonance, and second, to allow high oscillation mode drive levels without a significant DC heating contribution. Both of these goals are achieved with a circular resonator having electrostatic transducers.

The circular geometry is useful in that film access into the resonant space can be provided by a central hole with a minimal influence on the resonant modes. The azimuthal symmetry (and the nature of Bessel functions) allow for a rapidly diminishing intrusion of the hole upon the modes as the azimuthal mode number increases. Electrostatic transducers provide the amplitude accuracy and coupling efficiency. A traditional drive heater, which couples to third sound modes via the thermo-mechanical effect, delivers a DC heating on the order of 10^6 times larger than the AC power delivered to the resonant mode.[12] An electrostatic drive in principle will deliver energy only in response to the macroscopic motion of the helium dielectric. Similarly, an electrostatic pickup has a coupling to the wave motion that is directly calculable through electrostatics, whereas a bolometric detector has a sensitivity dependent on models of thermal coupling of the film to the substrate.

A schematic of the resonator is shown in Fig. 1. The region supporting the third sound resonance is formed by the surfaces in a 9.6 μm gap between two microscope slides, bounded by an epoxy filling in the gap external to the perimeter of a 6.15 mm radius circle. The 0.3 mm diameter hole pierces both plates along the axis of the circles. All of the inner surfaces are covered with approximately 200 nm of evaporated gold with the exception of small strips on one plate that had been masked during the evaporation and the epoxy perimeter. These serve to insulate sections of the gold film from one another, thus forming the drive and pickup capacitive electrodes with the opposite grounded plate. The outer surfaces are coated with about 400 nm of evaporated silver providing both electrical shielding and thermal contact to the glass plates. The resonator is spring-loaded against the bottom of a dilution refrigerator within a small chamber that includes a sintered silver film reservoir of approximately 20 m^2.

The pickup electrode senses the wave motion through the changes in capacitance associated with the flow of helium dielectric in and out of the
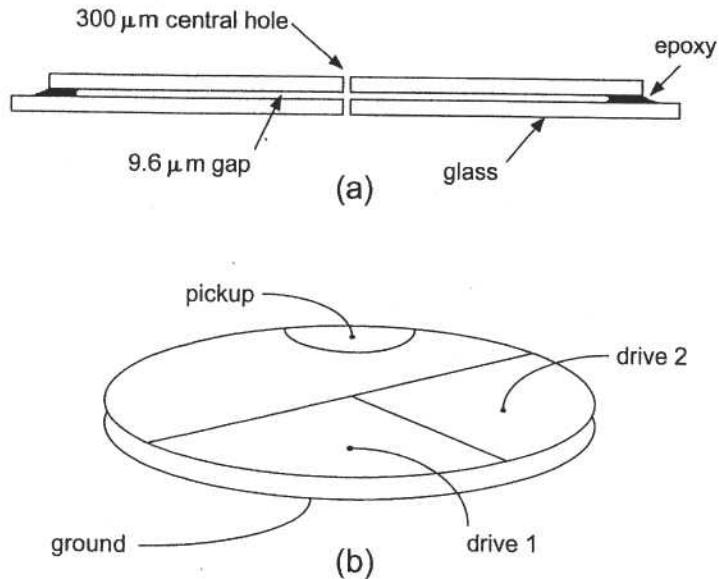
Fig. 1. (a) Cross section of the third sound resonator. The region between the plates and surrounded by epoxy forms the resonant cavity. Superfluid film enters through the small hole on the central axis. (b) Schematic of the drive and pickup electrodes evaporated in gold on the resonator's inner surface.

pickup region. The electrode capacitance serves as the capacitor of an L-C tunnel diode oscillator circuit that encodes the third sound displacement oscillations as a frequency modulation on a 76 MHz carrier. This signal is demodulated with room temperature electronics by phase locking the low temperature oscillator to an HP8656B synthesizer. A feedback signal required to accomplish this phase locking is then proportional to the third sound oscillations. All room temperature electronics are calibrated by known frequency modulations introduced into the reference synthesizer. Our knowledge of the wave amplitude is then dependent on characterizing the original L-C oscillator, ultimately determined by the inductance, the pickup capacitor area exposed to the resonance, the stray capacitance, and noise. The inductance and area are determined by room temperature measurements, and the stray capacitance (and subsequently the gap) are deduced by noting the frequency shift upon filling the resonator gap with bulk liquid.

The linearized resonant modes that couple to the transducers are symmetric with respect to the top and bottom plate and have wavenumbers given by $k_{m,n} = x_{m,n}/a$, where $x_{m,n}$ is defined through the Bessel function

TABLE I

Sensitivity of the Third Sound Resonator to the Modes Used in this Work. The Third and Fourth Columns Show Frequency Modulations About the 76 MHz Detector Carrier. The Third Column Lists the Response to the Given Mode Amplitude, and the Fourth Cites the Response to the Given Drive Voltage on Resonance

Mode(m, n)	$x_{m,n}$	Hz for $\delta h_0 = 1$ nm	Hz with a 1 V drive
(1, 1)	1.84118	150.2	9.6
(2, 1)	3.05424	111.4	6.4
(3, 1)	4.20119	83.4	2.6
(5, 1)	6.41562	40.8	0.90

condition $J'_m(x_{m,n}) = 0$ appropriate to the symmetric radial condition at the perimeter, and where a is the radius. The pickup electrode couples to each mode according to its overlap with the particular Bessel function involved. Sensitivities of the pickup to the modes are shown in Table I as frequency modulations in Hz of the 76 MHz carrier corresponding to a 1 nm mode amplitude, ($\delta h_0 = 1$ nm) in the expression for the film's surface elevation

$$h(r, \theta, t) = h_0 + \delta h_0 J_m(k_{m,n}r) \cos(m\theta) \cos(c_3 k_{m,n}t) \qquad (1)$$

in which h_0 is the quiescent film thickness. Also shown are the calculated modulation amplitudes on resonance for a 1 V (peak) drive acting on modes with a third sound speed of 10 m/s and $Q = 10^5$. It should be noted that at low amplitudes, where the linear theory is applicable, our measured responses agree with calculated responses to within 10%. Noise levels in the frequency modulation are typically 0.25 Hz within a 1 Hz bandwidth.

Film thicknesses are determined by the third sound speed c_3 and the relation

$$c_3^2(h_0) = \frac{h_0 - D}{h_0} \frac{3k_B T_v}{m_4 h_0^3} \qquad (2)$$

where m_4 is the helium mass and $D = 0.526$ nm accounts for the low temperature inactive components of the film. The strength of the van der Waals potential, $T_v = 41$ K, was determined by an independent film thickness measurement in another capacitor of evaporated gold in the same chamber.

The data acquisition procedure involves driving up a particular mode to some high amplitude and then recording the amplitude and frequency of the resonance signal as the mode decays away.

Before the drive-up, the low amplitude free decay frequency is verified. This low amplitude value is used as the fixed reference frequency for an

SR530 two phase lock-in amplifier. During the drive-up, higher amplitudes are achieved by shifting the drive frequency by as much as a few tenths of a Hertz lower than the linear resonance, closer to where the peaks of non-Lorentzian high amplitude lineshapes are observed.

The drive is then turned off, and the two phases of the lock-in output are recorded. With the lockin referenced to the fixed low amplitude resonance, the two signal phases experience beats with the reference at high amplitudes where the signal frequency is shifted. The beats can be interpreted as the components of the complex signal amplitude rotating at the difference frequency between the free decay and the reference. Much attention is given to the gain and averaging time during the decay to ensure that this signal is not distorted. Fortunately, the amplitude is large when there is significant dynamical behavior in the signal (rapid beats and a relatively fast decay), so little averaging is necessary, and as the signal decays toward the noise, both the decay rate and the frequency difference beats become compatible with a significantly longer averaging time. Data is taken at a rate coupled to the lock-in averaging time.
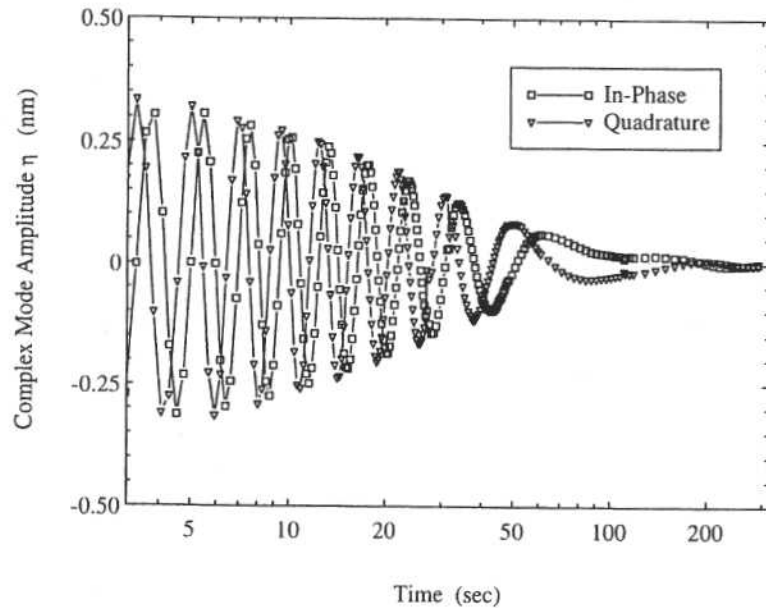

Fig. 2. In-phase and quadrature lock-in output channels during the free decay of a third sound resonance (with $m = 2$ and $c_3 = 14.9$ m/s). The vertical scale has been converted to thickness amplitude components. Note that, for clarity, the time axis is shown with a logarithmic scaling. Frequency deviations from the lock-in reference show up as oscillations in the two channels.

A plot of the lockin output data is shown in Fig. 2, scaled to give the mode amplitude δh_0 using the calibration signal from the phase locked loop synthesizer and the appropriate sensitivity from Table I. Note that the oscillation cycles represent the frequency shift Δf of the free decay resonance from the reference fixed at the low amplitude value f_0, and the amplitude represents the mode oscillation amplitude δh_0. These quantities are extracted from the curves in Fig. 2 and plotted as a relative frequency shift ($\Delta f/f_0$) vs. the square of amplitude relative to the film thickness ($\delta h_0/h_0$) in Fig. 3.

The decay in Fig. 3 proceeds from right to left on the graph. Note the significant region of quadratic behavior (straight line on the graph) extending into the low amplitude region at the left. All of the modes that we have observed display this quadratic region. The frequency shift data can therefore be characterized by one number: the slope of the plots analyzed as in Fig. 3. We shall call this slope β, defined where the free decays are described by

$$\frac{\Delta f}{f_0} = \beta \left(\frac{\delta h_0}{h_0} \right)^2 \qquad (3)$$

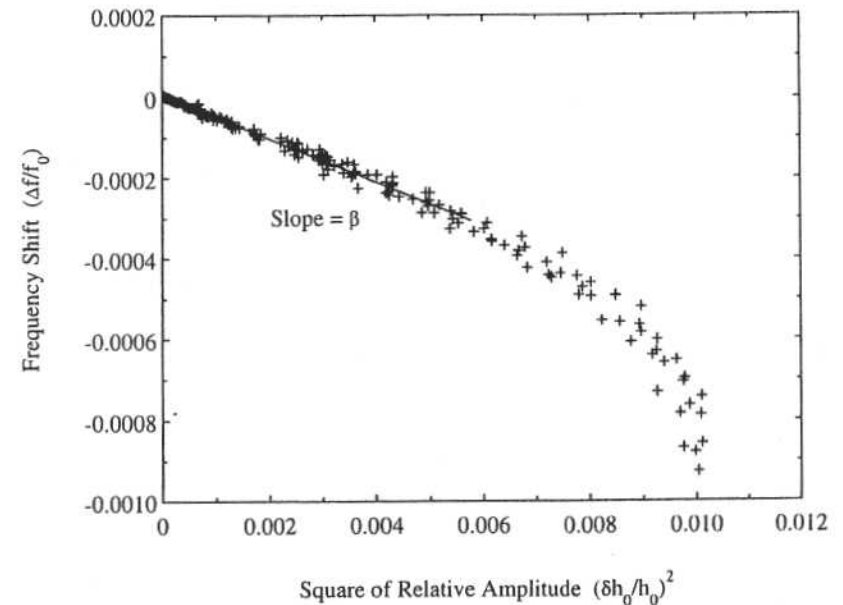The numbers β depend on the mode and the film thickness.

Fig. 3. The data of Fig. 2 analyzed into both frequency shift and resonance mode amplitude. The decay proceeds in time from right to left. The slope of the low amplitude limit of the data is defined as β.

Figure 4 summarizes the results for $m = 1, 2, 3$ and 5 at several different film thicknesses. Most of the measurements were made at a temperature of 0.06 K. No temperature dependence in the values for β was observed up to 0.3 K in spite of a reduction in the resonance Q of typically more than a factor of two in this range. The error bars represent our estimate for the uncertainty in the values based on our uncertainty in the film thickness and the variability of the calibration value. Calibrations were performed before and after a set of decays and most likely owe their variation to changes in the DC state of the phase locked loop. These values of β are the only
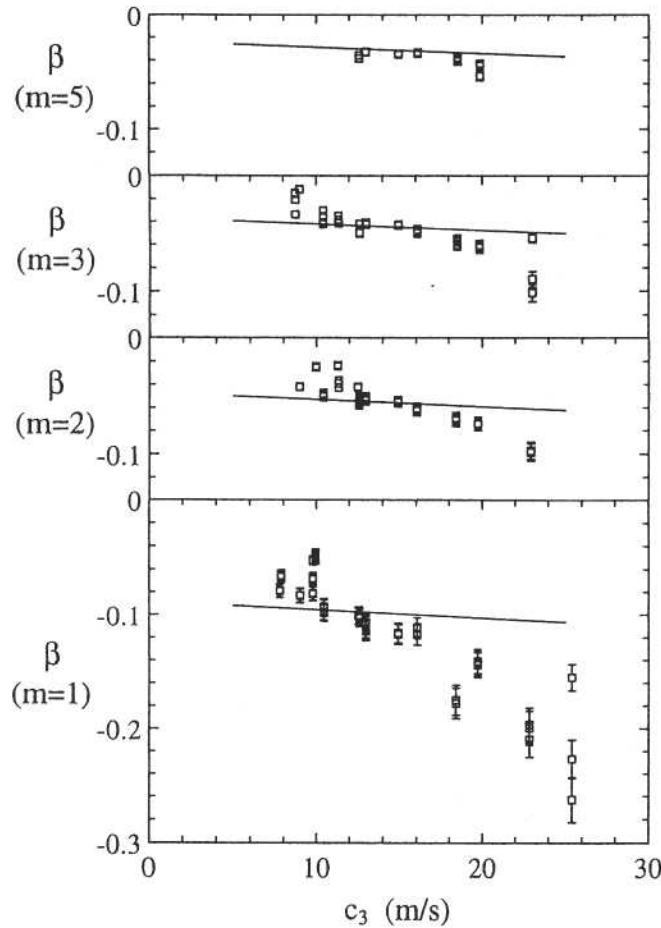

Fig. 4. Values of β determined for a variety of film thicknesses and modes. The solid line shows the theoretical prediction. The vertical scale in all plots is fixed for comparison.

feature of the decays to which the theory will be compared, with the assumption that the observed quadratic behavior is the lowest amplitude manifestation of the nonlinear fluid mechanics in the film.

THEORY

Our basic equations for the film come from the standard two-fluid model:[13] the equation of continuity,

$$\frac{\partial h}{\partial t} = -\operatorname{div}[(h - D)\mathbf{v}] \tag{4}$$

and the dynamical equation,

$$\frac{\partial \mathbf{v}}{\partial t} + (\mathbf{v} \cdot \operatorname{grad})\mathbf{v} = -\frac{dU}{dh}\operatorname{grad} h \tag{5}$$

The symbol h denotes the film thickness; $\mathbf{v}$, the superfluid velocity field; and U, the van der Waals potential energy per atom (divided by the mass of a helium atom). In effect, superfluid flows only in a layer sandwiched between a healing length at the top of the film and another healing length immediately above the frozen first atomic layer. The constant D, taken to be 1.47 atomic layers, represents the healing lengths and the frozen layer. The experiments were done at temperatures of order 0.1 K, where a temperature gradient in the dynamical equation should be negligible and hence is omitted. Moreover, the experimental values of showed no variation with temperature over the experimental temperature range.

Dimensionless variables make the computation easier, and so we introduce a set of them. Let h_0 denote the thickness of the quiescent film. The third sound speed c_3 is given by

$$c_3^2 = bh_0 \left. \frac{dU}{dh} \right|_{h_0} \tag{6}$$

where b, defined by

$$b \equiv \frac{h_0 - D}{h_0} \tag{7}$$

incorporates the effect of the inactive layers. We write

$$h = h_0 + \alpha h_0 \eta \tag{8}$$

$$\mathbf{v} = \frac{c_3}{b} \alpha \mathbf{u} \tag{9}$$

The scaling constant α represents the maximum wave amplitude divided by h_0; the function $\eta(r, \theta, t)$ is a dimensionless wave amplitude (whose magnitude is of order unity); and $\mathbf{u}$ is a dimensionless velocity field. The standard van der Waals potential energy $U(h)$ varies with h as h^{-3} for films of our thickness. We write

$$\frac{dU(h)}{dh} = \frac{dU}{dh}\bigg|_{h_0} f\left(\frac{h}{h_0}\right) \tag{10}$$

where

$$f\left(\frac{h}{h_0}\right) = \left(\frac{h}{h_0}\right)^{-4} \tag{11}$$

When we rewrite Eqs. (4) and (5), we measure length in units of the cell radius a and time in units of a travel time for third sound: a/c_3. The outcome is the following pair of equations:

$$\frac{\partial \eta}{\partial t} = -\operatorname{div}\left[\left(1 + \frac{\alpha}{b}\eta\right)\mathbf{u}\right] \tag{12}$$

$$\frac{\partial \mathbf{u}}{\partial t} = -\frac{1}{2}\frac{\alpha}{b}\operatorname{grad}(\mathbf{u}\cdot\mathbf{u}) - f(1 + \alpha\eta)\operatorname{grad}\eta \tag{13}$$

The irrotational character of the superfluid velocity permits us to re-express the advective derivative in terms of a pure gradient.

The theoretical goal is to extract from Eqs. (12) and (13) a frequency shift that is proportional to α^2. Two papers by John Miles (Refs. 11 and 14) provided inspiration and guidance. Following Miles, we expand η and $\mathbf{u}$ in terms of the film's normal modes, that is, in terms of the solutions to the linearized forms of Eqs. (12) and (13). Thus we write

$$\eta = \sum_n \eta_n(t)\,\psi_n(r, \theta), \tag{14}$$

$$\mathbf{u} = \sum_n \varphi_n(t)\,\mathbf{U}_n(r, \theta) \tag{15}$$

where

$$\mathbf{U}_n = \omega_n^{-1}\operatorname{grad}\psi_n \tag{16}$$

The symbol ω_n denotes the (dimensionless) eigenfrequency of the linearized theory. The set of frequencies $\{\omega_n\}$ includes the set $\{x_{m,n}\}$ of Table I but

in a compressed and different notation. The eigenfunctions ψ_n are constructed to be orthonormal, and so are the basis vectors $\mathbf{U}_n$.

The construction of the normal modes requires, however, a specification of boundary conditions. The reflection symmetry of the experimental cell (top and bottom) strongly suggests that no fluid runs from one face to the other, and so

$$\mathbf{r}\cdot\mathbf{U}_n|_{r=1} = 0 \tag{17}$$

is required at the outer radius. If we mentally paper over the tiny central hole in each face, then that boundary condition suffices. We will find, however, that we need to acknowledge the hole. When we do so, we will need to use the normal modes of a larger system: cell plus exterior. Computing those modes, even in an approximate fashion, is a subtle matter and will be given its proper discussion later.

To give a concrete example of an eigenfunction, let us first cover up the hole; then an example is

$$\psi_1(r, \theta) = N_1 J_{m_1}(\omega_1 r)\cos(m_1\theta) \tag{18}$$

where the integer m_1 specifies the azimuthal dependence and N_1 is a normalization constant. Each such function with a cosine azimuthal dependence is paired with a similar function that has a sine dependence. The mode whose frequency shift is being investigated will be designated by the subscript 1 and is one member of the "primary pair." The partner in the primary pair is denoted by subscript 2. (Thus the numerical values of m_1 and m_2 are equal. For the mode described in the experimental section as the "(5, 1)" mode, the values are $m_1 = m_2 = 5$.)

Most of the ensuing algebra is best left to a computer; we used the symbolic manipulation software *Mathematica*®. Here we merely outline the method verbally and then present results, both analytic and numerical. The method itself is independent of the particulars of the normal modes; those specific details affect only the numerical outcome.

We substitute the forms for η and $\mathbf{u}$ from Eqs. (14) and (15) into Eqs. (12) and (13), expand the function $f(1 + \alpha\eta)$ through order α^2, multiply Eq. (12) by ψ_i and take the scalar product of Eq. (13) with $\mathbf{U}_i$, and finally integrate over the film area (a disk or a model of cell plus exterior). The operations project out equations for $\dot{\eta}_i$ and $\dot{\varphi}_i$, where the dot denotes differentiation with respect to time.

One can solve the projected version of Eq. (12) iteratively for φ_i as a power series in α with coefficients dependent on the set $\{\eta_n, \dot{\eta}_n\}$. We work through order α^2. Then we use the series to replace all occurrences of φ_i

and $\dot{\varphi}_j$ in the projected version of Eq. (13) in terms of η_j and $\dot{\eta}_j$. Symbolically, projection from Eq. (13) generates the set of equations

$$F_i(\{\eta_n, \dot{\eta}_n, \ddot{\eta}_n\}) = 0 \qquad (19)$$

where each F_i denotes a known but lengthy function.

We follow Miles in adopting forms for the coefficients η_n. Let $n = 1$ and ψ_1 denote the low-amplitude limit of the actual large-amplitude wave. We write

$$\eta_1(t) = p_1(\tau) \cos(\bar{\omega}t) + q_1(\tau) \sin(\bar{\omega}t) \qquad (20)$$

where

$$\tau = \tfrac{1}{2}\alpha^2 t \qquad (21)$$

The waves of the linearized limit come in cosine and sine pairs, as noted in conjunction with Eq. (18). Ideally, the two modes are degenerate in frequency, but experimental imperfections produce a geometric splitting (fractionally, of order 10^{-3} to 10^{-4}). The symbol $\bar{\omega}$ denotes the mean of the split frequencies. If there were no nonlinear interactions (and no geometric splitting), then the functions p_1 and q_1 would be constant in time. In reality, p_1 and q_1 vary slowly with time; the desired frequency shift will appear as part of that slow variation. A form similar to that in Eq. (20) holds for the other mode in the primary pair, which we enumerate with $n = 2$.

The nonlinear terms in Eqs. (12) and (13) will generate secondary waves with azimuthal dependence like $\cos(2m_1\theta)$ and $\cos(\text{zero})$ and also time dependence like $\cos(2\bar{\omega}t)$ and $\cos(\text{zero})$. For the secondary modes that are thus excited by the primary mode $\eta_1\psi_1$, we take the form

$$\eta_n = \alpha[A_n \cos(2\bar{\omega}t) + B_n \sin(2\bar{\omega}t) + C_n] \qquad (22)$$

The computer solves the secondary equations in Eq. (19) for the coefficients $\{A_n, B_n, C_n\}$ of the secondary modes, expressing those coefficients in terms of the set $\{p_n, q_n\}$. Then the program substitutes those "known" coefficients into the primary equations in Eq. (19) and extracts differential equations for the set of functions $\{p_n, q_n\}$. The outcome has an algebraic structure that can be expressed succinctly. Let

$$r_n = p_n + iq_n \qquad (23)$$

for the primary modes, $n = 1$ and 2. Then the nonlinear differential equations are these:

$$\frac{dr_1}{d\tau} = BMr_2 + iAEr_1 - i\zeta r_1 \qquad (24)$$

$$\frac{dr_2}{d\tau} = -BMr_1 + iAEr_2 + i\zeta r_2 \qquad (25)$$

The constant ζ is proportional to the geometric splitting. The functions E and M are defined by

$$E = E_1 + E_2 \equiv \sum_{n=1}^{2} \tfrac{1}{2}(p_n^2 + q_n^2) \qquad (26)$$

and

$$M = p_1 q_2 - p_2 q_1 \qquad (27)$$

The energy and angular momentum of the wave have expansions in powers of α. The functions E and M are proportional to the terms of lowest order (that is, order α^2) in those series, respectively. The function E is a constant of the motion for Eqs. (24) and (25); in the absence of geometric splitting, the function M would also be a constant of the motion. The numerical constants A and B are provided by the computer program.

If only one of the primary modes is excited, then the angular momentum M is zero and remains so. The solution of Eq. (24) is then

$$\eta_1(t) = p_1(0) \cos\{[\bar{\omega} + (\zeta - AE)\tfrac{1}{2}\alpha^2]t\} \qquad (28)$$

provided one sets the clock so that $q_1(0) = 0$. A frequency shift proportional to $-0.5AE\alpha^2$ emerges plainly. Indeed, from the definition of β and from Eqs. (8), (14), (18), and (28), one finds

$$\beta = -\frac{A}{4\bar{\omega}N_1^2} \qquad (29)$$

The foregoing paragraphs lay out the theoretical framework. What remains to be done is to insert specific normal modes and to work out the numerical results. Here we present an outline of the next two subsections and the two appendices.

In the subsection "Results for the disk," we suppress the possibility that fluid may move through the central hole and consider the normal modes for a film on a disk. (Our original hope—if not expectation—was that this model would suffice.) We describe a check on the computer coding, present some numerical results (based on the van der Waals restoring force), and explain (in part) why the theoretical results disagree with experiment.

In the subsection "Results for the annulus," we allow fluid to move through the hole in dynamic response to the oscillations in the cell. We describe a geometric model of cell plus exterior (but leave the details of the normal modes to Appendix A). The numerical results are summarized by the theoretical lines in Fig. 4.

In Appendix B, entitled "Analysis by Bernoulli's principle," we provide a more intuitive understanding of why the average film thickness in the cell changes and how that change shifts the frequency.

Our conclusions are presented after the subsection "Results for the annulus."

Results for the Disk. If we mentally paper over the central hole, then we can readily check the present calculation against Miles's results for gravity waves on water. We need only set $b = 1$ and take $f(1 + \alpha\eta) = f(1) = 1$, a constant restoring force. In the limit of vanishing water depth, Miles's results imply $\beta = -0.132$ when $m_1 = 1$; the route via *Mathematica* concurs.

Next, we restore the variation with height of the van der Waals attraction and expand $f(1 + \alpha\eta)$ through order α^2:

$$f(1 + \alpha\eta) = 1 - 4\alpha\eta + 10\alpha^2\eta^2 \qquad (30)$$

Also, we restore the influence of the inactive layers. For $m_1 = 1$ and $c_3 = 10$ m/s, the computer program implies $\beta = +0.012$, wildly at variance with the experimental result that all β's are negative. Moreover, the "wrong sign" outcome persists for higher values of m_1, and it is not a consequence of our including too few modes. [Typically, we compute with the pair of primary modes (and their first Bessel functions), the pair of modes with azimuthal dependence $2m_1\theta$ (and their first Bessel functions), and the lowest *three* axisymmetric modes.]

A look at Eqs. (13) and (30) reveals a source of the discrepancy. As the coefficient of grad η, the function $f(1 + \alpha\eta)$ plays the role of a variable "spring constant." The term in $+10\alpha^2\eta^2$ clearly hardens the spring and hence tends to increase the oscillation frequency; that is, the term contributes positively to β. The effect of the term in $-4\alpha\eta$ cannot be assessed by inspection, for η changes sign periodically, and the sign of some appropriate mean value is not obvious (at least, not to us). Numerical test, however, shows that the term in $-4\alpha\eta$ softens the spring. The net effect of the two terms, however, is dominated by the term $+10\alpha^2\eta^2$. Thus, in this case, the curvature of the van der Waals force (as a function of height) dominates over the slope.

Confronted with such disagreement over the sign of β, we conclude that we must acknowledge the central hole and explore its implications.

Results for the Annulus. If helium flows into the cell in response to a growing amplitude of oscillation, then the time-averaged film thickness will become greater, the average van der Waals force will be less, the oscillation frequency will drop, and β will be negative. That is a plausible scenario, but how should one approach it theoretically?

In principle, one should calculate the normal modes of the entire interconnected system: cell, holes, helium reservoir, and associated capillary tubes. Clearly, that is impossible. A tractable model can be based on Fig. 1. A "cell" annulus (representing one face of the cell's interior) is connected to a short hollow cylinder that, in turn, is connected to a large "exterior" annulus (representing one half of the exterior). The boundary conditions are that the radial component of the fluid velocity must vanish at the outer edge of each annulus. The radius of the exterior annulus is r_{ext}, which is much larger than the unit value of the cell's outer radius. For the cylinder, the ratio of length to radius is 7.5.

For all practical purposes, the modes of the original disk with $m \neq 0$ remain confined to the cell annulus. Any such mode is a superposition of circulating waves, and a centrifugal effect keeps the bulk of the mode out of the hollow cylinder. [Within the cylinder, the wave amplitude drops exponentially with an e-folding length of (hole radius)/m.] The eigenfrequencies change extremely little (fractionally, of order 10^{-7} or less), and the eigenfunctions change little also [because the regular Bessel functions $J_m(\omega r)$ already vanish at the origin]. Only for the axisymmetric modes is there substantial change.

Appendix A outlines the methods that we used to compute the axisymmetric modes of the model system. Here we present merely certain results.

For the disk (that is, for the cell when the hole is "covered"), the first and second significant axisymmetric modes have frequencies of $\omega = 3.832$ and 7.016, respectively. (The perfectly flat mode has $\omega = 0$ and is not dynamically significant.) In the model, the frequencies of the first and second disk modes shift upward by only 3 percent and 1 percent, respectively, and so the shapes of the modes (within the cell) change hardly at all.

The striking result is that an entirely new dynamically-significant axisymmetric mode arises. Its frequency is $\omega \cong 0.35$. Within the cell, its profile is approximately that of a quarter-circle: a nearly vertical tangent at the edge of the hole and a horizontal tangent at the outer edge of the annulus. At the edge of the hole, the wave height is 79 percent of the maximum that the wave achieves at the outer edge. Thus, when this secondary mode is driven by the primary mode, its DC portion will raise the average level of the helium in the cell (an average taken in both time and space). That will reduce the average van der Waals force, causing the oscillation

frequency of the dominant mode to drop; consequently, the interaction of the modes will make a negative contribution to β. The detailed computations bear out this qualitative expectation, as Fig. 4 shows.

A rigorous and explicit derivation of the rise in the average film thickness is presented in Appendix B. The appendix complements both the preceding paragraph and also the numerical analysis that is based on the perturbation theory in Eqs. (19) to (30).

CONCLUSIONS

We have experimentally determined nonlinear behavior by observing an unambiguous quadratic dependence of the resonance frequency shifts upon amplitude. As a function of film thickness, the results of Fig. 4 show a systematic deviation between theory and experiment, particularly with the $m = 1$ mode in the thinner films. Nonetheless, the extent of agreement is significant, as we reason in the following paragraphs.

Several nonlinear terms in Eqs. (12) and (13) contribute to β: the term in div$(\eta\mathbf{u})$; the term in grad$(\mathbf{u} \cdot \mathbf{u})$; and two terms from the expansion of $f(1 + \alpha\eta)$, as displayed in Eq. (30). Numerical investigation tells us that, if either of the terms from $f(1 + \alpha\eta)$ were to be omitted, the prediction for β would fall well outside the experimental range. The contributions of those two terms are, in fact, delicately balanced and nearly cancel each other. Moreover, their contributions turn out to be independent of each other's presence in the equations. In a sense, the bulk of the net value of β comes from the terms in div$(\eta\mathbf{u})$ and grad$(\mathbf{u} \cdot \mathbf{u})$, acting together. Such details are not important in themselves, but they indicate that the net frequency shift arises as the collective effect of several nonlinear terms.

The individual terms in the theory make contributions $\Delta\beta$ that span the range $-0.25 < \Delta\beta < 0.25$. Thus 0.5 sets the scale for comparison between theory and experiment. In general, theory and experiment agree within 10% of that scale. The sole exception is the $m = 1$ mode above 20 m/s, where the deviation climbs to 30%. The trend toward positive movement of β with both increasing m and increasing film thickness is clearly present in both theory and data. From all this evidence we infer that a straight forward application of classical hydrodynamics accounts for the bulk of the nonlinear influences within the film.

This result is significant in that we have justified the use of these nonlinear terms in an experimental situation in which the dispersive nature of the superfluid film is inconsequential. Previous treatments, both experimental and theoretical, have been within the context of solitary waves, where the nonlinear behavior is equally influenced by dispersion. Our insensitivity

to dispersion is a result of the mode structure of the circular resonator. The near perfect 2:1 simultaneous resonances in both k and ω characteristic of rectangular, or plane waves, are avoided.

We have also brought to light the importance of the low frequency mode structure of the third sound geometry. As shown, the film in the vicinity of third sound wave activity may be thickened to an extent determined by this mode structure, ranging from a completely isolated resonator in which there is no such mode, to a resonator that is free to exchange helium with an infinite reservoir. Both the relative sizes of the film regions and the geometry of the flow connections influence this mode structure. In the case of pulsed third sound, the localized nature of the wave excitation (as opposed to the infinite plane wave pulse) will include both linear and nonlinear coupling to any extended modes of the experimental geometry. This coupling must be considered as a possible contributing factor to the complex behavior observed following third sound pulses.

APPENDIX A: NORMAL MODES

In this appendix, we outline the methods that we used to compute the axisymmetric modes of the model system. The calculation proceeds in two stages, as follows.

Stage 1. Temporarily, we ignore the boundary condition at $r = r_{ext}$ and take r_{ext} to be extremely large. We look for the resonances of this system by sending inward (on the exterior annulus) an axisymmetric wave of frequency ω and requiring an outgoing wave of equal amplitude but perhaps shifted in phase. Thus, on the exterior annulus, we represent the film height by

$$\psi_{ext} = \text{Re}\{ [H_0^{(2)}(\omega r) + e^{i\varphi} H_0^{(1)}(\omega r)] e^{-i\omega t} \} \tag{A1}$$

where the radial dependence is expressed by Hankel functions and φ is an adjustable phase constant. A function ψ_{cyl} must match with ψ_{ext} in value and slope at the exterior end of the hollow cylinder. Simultaneously, a function ψ_{cell} must match with ψ_{cyl} at the hole and must meet the boundary condition at $r = 1$. The latter function is

$$\psi_{cell} = \text{Re}\left\{ A_{cell} \left[J_0(\omega r) - \frac{J_0'(\omega)}{Y_0'(\omega)} Y_0(\omega r) \right] e^{-i\omega t} \right\} \tag{A2}$$

where A_{cell} is an adjustable (possibly complex) constant.

We vary the frequency ω and so produce the resonance graph shown in Fig. 5. The new mode at $\omega \cong 0.35$ stands out dramatically. At the resonant peaks, one finds $\exp(i\varphi) \cong -1$ to good accuracy, and so the combination of Hankel functions in Eq. (A1) reduces approximately to $-2iY_0(\omega r)$. This information and Fig. 5 enable us to construct approximate normal modes of the model system. The nth such mode has the representation (in the respective regions)

$$\psi_n(r, \theta) = \text{NormC}_n \times \begin{cases} f_{n,\text{cell}} \\ f_{n,\text{cyl}} \\ f_{n,\text{ext}} \cong S_n Y_0(\omega_n r) \end{cases} \tag{A3}$$

The function $f_{n,\text{cell}}$ is proportional to the r-dependent factor in ψ_{cell} as displayed in Eq. (A2) and is normalized to unity over the cell annulus. The height of the resonance in Fig. 5 then enables us to determine the numerical value of the scaling constant S_n. The overall normalization constant NormC_n is determined by requiring that the integral of $|\psi_n|^2$, taken over the entire model area, be unity. Provided $r_{\text{ext}} \gg 1$, the integral is dominated by the integral of $(S_n Y_0)^2$, and that integral is asymptotically equal to $2\omega^{-1} S_n^2 r_{\text{ext}}$. Thus NormC_n is proportional to $r_{\text{ext}}^{-1/2}$.
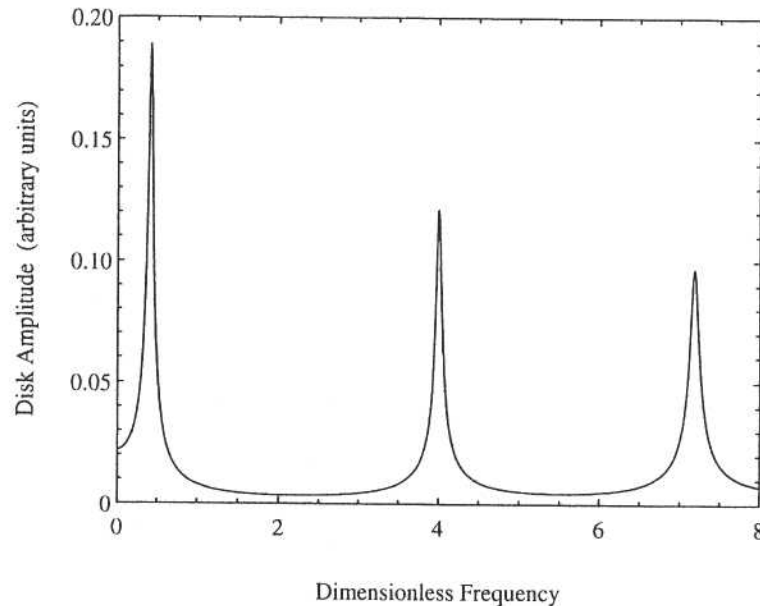

Fig. 5. The resonant response of the cell amplitude A_{cell} as a function of frequency.

We have not yet incorporated the boundary condition at $r = r_{\text{ext}}$. The asymptotic form of a more accurate expression for ψ_{ext} will be

$$f_{\text{ext}} \approx S_n \left(\frac{2}{\pi \omega r}\right)^{1/2} \sin(\omega r + \text{phase}) \tag{A4}$$

The boundary condition requires that $df_{\text{ext}}/dr = 0$ at $r = r_{\text{ext}}$. If this condition is met for one value of ω, then it will be met also by values of ω that differ additively by $\pm \pi/r_{\text{exp}}$ (provided that the term "phase" varies little with ω). The quotient π/r_{ext} is a very small number. Consequently, under a resonance such as any of the three displayed in Fig. 5, there will be a discrete sequence of normal modes. The "density of states" $d\Omega/d\omega$ for the modes is

$$\frac{d\Omega}{d\omega} = \frac{r_{\text{ext}}}{\pi} \tag{A5}$$

Thus the model provides not a single mode for each resonance but a set of modes. The frequencies differ by little, however, and the wave shapes within the cell, that is, the functions $f_{n,\text{cell}}$, differ hardly at all. For the sake of computing β, we may collect together all the discrete modes under a specific resonance. Whenever a sum over secondary modes is called for, we may handle the axisymmetric modes by summing over the resonances, using at each resonance the discrete mode with the maximum cell amplitude and incorporating the effect of the subsidiary modes by multiplying by an effective number of modes, $\text{effN}_{i\text{th res}}$. We estimate the latter by

$$\text{effN}_{i\text{th res}} = \frac{d\Omega}{d\omega} \times \text{FWHM}_{i\text{th res}} = \frac{r_{\text{ext}}}{\pi} \times \text{FWHM}_{i\text{th res}} \tag{A6}$$

where $\text{FWHM}_{i\text{th res}}$ denotes the full width at half maximum of the ith resonance shown in Fig. 5.

Detailed inspection of the procedures discussed in the paragraphs following Eq. (18) shows that β depends on NormC_n and $\text{effN}_{i\text{th res}}$ through the combination $(\text{NormC}_n)^2 \times \text{effN}_{i\text{th res}}$ only. (Here NormC_n is the normalization constant for the discrete mode with maximum amplitude in the ith resonance.) Because NormC_n is proportional to $r_{\text{ext}}^{-1/2}$, the essential combination of factors is independent of r_{ext}. That is gratifying, for once the exterior is large relative to the cell, then precisely how large it is should not matter.

Stage 2. To confirm the conclusions of the preceding analysis and to refine the estimates of effN$_{i\text{th res}}$, we imposed the boundary condition at $r = r_{\text{ext}}$ exactly and computed numerically the spectrum of normal modes when $r_{\text{ext}} = 1000$. The densities of states agree with Eq. (A5) to within one percent. We could assess effN$_{i\text{th res}}$ by summing over the modes under a resonance, weighting each mode by the square of its NormC (normalized by the NormC for the mode at the peak). This assessment of effN$_{i\text{th res}}$ is 15 to 20 percent smaller than the stage 1 assessment, and we used the better (and smaller) values. The normalization constant NormC$_n$ is proportional to the height of the resonance; the stage 1 and stage 2 assessments of the resonance height agree to within one percent for all three resonances. In short, the methods agree well, and all differences have little effect on the theoretical value of β.

APPENDIX B: ANALYSIS BY BERNOULLI'S PRINCIPLE

Bernoulli's principle, suitably generalized to a temporally periodic system, enables one to derive the increase in the average film thickness within the cell. Under the specification that the fluid is irrotational, Eq. (5) can be written as

$$\frac{\partial \mathbf{v}}{\partial t} = -\frac{1}{2}\,\text{grad}\,v^2 - \text{grad}\,U(h) \tag{B1}$$

Averaging over one period of the periodic motion reduces the left hand side to zero. Thus

$$\tfrac{1}{2}\langle v^2 \rangle + \langle U(h) \rangle = C_1 \tag{B2}$$

where the angular brackets denote a temporal average and where C_1 is a constant (in both space and time). This expression is the generalized Bernoulli's principle.

The next objective is to extract $\langle \eta \rangle_{\text{time \& cell}}$, the thickness variation when averaged over both time and the cell. To that end, expand the potential $U(h)$ through second order in $\alpha h_0 \eta$ and use the notation of Eqs. (6) to (9), finding that Eq. (B2) becomes

$$\frac{1}{2b}\left[\langle u^2 \rangle + b\,\frac{U''(h_0)h_0}{U'(h_0)}\langle \eta^2 \rangle \right] + \alpha^{-1}\langle \eta \rangle = C_2 \tag{B3}$$

where C_2 is a new constant.

The temporal average $\langle \eta \rangle$ must be of order α because the part of η that is of order α^0 is purely oscillatory. Thus, to determine $\alpha^{-1}\langle \eta \rangle$, it suffices to know the other quantities in Eq. (B3) to order α^0. In particular, the terms in $\langle u^2 \rangle$ and $\langle \eta^2 \rangle$ need be used in order α^0 only.

To determine the constant C_2, integrate Eq. (B3) over the entire film area—cell, hollow cylinder, and exterior—and invoke conservation of fluid, which requires the integral of η over the entire area to be zero. Let $G(\mathbf{x})$ denote the expression in square brackets in Eq. (B3), together with its prefactor, but evaluated to order α^0 only, that is, evaluated with just the dominant mode. Because the dominant mode is restricted to the cell, $G(\mathbf{x})$ is non-zero only inside the cell. Thus spatial integration of Eq. (B3) over the entire area yields

$$C_2 = \int_{\text{cell}} G\, dA / A_{\text{total}} \tag{B4}$$

where A_{total} denotes the total area of cell, cylinder, and exterior.

Now return to Eq. (B3) and integrate over the cell only. Using Eq. (B4) as well, one finds

$$\langle \eta \rangle_{\text{time \& cell}} = -\frac{\alpha \langle \eta^2 \rangle_{\alpha=0,\,\text{time \& cell}}}{2b}\left[1 + b\,\frac{U''(h_0)h_0}{U'(h_0)} \right] \times \frac{A_{\text{total}} - A_{\text{cell}}}{A_{\text{total}}} \tag{B5}$$

Here A_{cell} denotes the cell area. In lowest order, the dominant mode is like an harmonic oscillator, and so the averages of u^2 and η^2 are equal in order α^0; this enables one to replace the u^2 average by the η^2 average.

By Eqs. (10) and (11), the expression in square brackets in Eq. (B5) is $[1 - 4b]$. Because $b \geqslant 0.8$ for our films, the expression $[1 - 4b]$ is negative, and so $\langle \eta \rangle_{\text{time \& cell}}$ is positive. On average, the film in the cell has become thicker.

For the relative frequency shift, we can argue loosely as follows. The frequency ω will have the form

$$\omega = (\text{geometric factor}) \times c_3/a \tag{B6}$$

The revised third sound speed (squared) is given by

$$c_3^2 \cong b\left(\frac{h\,dU}{dh} \right)\bigg|_{h_0 + h_0\alpha\langle \eta \rangle_{\text{time \& cell}}} \tag{B7}$$

Expanding to first order in α and then taking a square root give the revised speed:

$$c_3 \cong (1 - \tfrac{3}{2}\alpha\langle \eta \rangle_{\text{time \& cell}}) \times c_3|_{\alpha=0} \tag{B8}$$

The relative frequency shift follows now from Eqs. (B6, B8, & B5) as

$$\frac{\Delta\omega}{\omega} \cong -\frac{3}{2}\alpha\langle\eta\rangle_{\text{time \& cell}}$$

$$\cong -\frac{9}{4}\frac{\langle(h-h_0)^2\rangle_{\text{time \& cell}}}{h_0^2} \qquad (B9)$$

In basic structure, sign, and order of magnitude, this expression corroborates the result from the detailed analysis.

ACKNOWLEDGMENTS

REFERENCES

1. D. J. Bergman, *Phys. Rev.* **188**, 370 (1969).
2. M. Ichiyanaga, *Physics Lett.* **55A**, 283 (1975).
3. B. A. Huberman, *Phys. Rev. Lett.* **41**, 1389 (1978).
4. C. A. Condat, and R. A. Guyer, *Phys. Rev. B* **25**, 3117 (1982).
5. K. Kono, S. Kobayashi, and W. Sasaki, *J. Phys. Soc. Japan* **50**, 721 (1981).
6. M. J. McKenna, R. J. Stanley, E. DiMasi, and J. D. Maynard, *Physica B* **165+166**, 603 (1990).
7. K. S. Ketola, S. Wang, and R. B. Hallock, *Physica B* **194-196**, 649 (1994).
8. V. A. Hopkins, J. Keat, G. D. Meegan, T. Zhang, and J. D. Maynard, *Phys. Rev. Lett.* **76**, 1102 (1996).
9. F. M. Ellis and H. Luo, *J. Low Temp. Phys.* **89**, 115 (1992).
10. A. R. Osborne, *Phys. Rev. E* **52**, 1105 (1995).
11. J. W. Miles, *J. Fluid Mech.* **75**, 419 (1976).
12. F. M. Ellis, and R. B. Hallock, *Rev. Sci. Instrum.* **54**, 751 (1983).
13. K. R. Atkins and I. Rudnick, *Progress in Low Temperature Physics, Vol. VI*, C. J. Gorter (ed.), North-Holland, Amsterdam (1970), chapter 2.
14. J. W. Miles, *J. Fluid Mech.* **149**, 15 (1984).